Backbone Dynamics of Apocytochrome b_5 in Its Native, Partially Folded State†

Shibani Bhattacharya, Christopher J. Falzone, and Juliette T. J. Lecomte*

Department of Chemistry, The Pennsylvania State University, University Park, Pennsylvania 16802

Received September 25, 1998; Revised Manuscript Received December 23, 1998

ABSTRACT: The backbone dynamics in the native state of apocytochrome b_5 were studied using ^{15}N nuclear magnetic spin relaxation measurements. The field (11.7 and 14.1 T) and temperature (10−25 °C) dependence of the relaxation parameters (R_1, R_2, and $R_{1\rho}$) and the ^{1}H−^{15}N NOE established that the protein undergoes multiple time scale internal motions related to the secondary structure. The relaxation data were analyzed with the reduced spectral density mapping approach and within the extended model-free framework. The apoprotein was confirmed to contain a disordered heme-binding loop of approximately 30 residues with dynamics on the sub-nanosecond time scale ($0.6 < S^2 < 0.7$, 100 ps $< \tau_e <$ 500 ps). This loop is attached to a structured hydrophobic core, rigid on the picosecond time scale ($S^2 > 0.75$, $\tau_e <$ 50 ps). The inability to fit the data for several residues with the model-free protocol revealed the presence of correlated motion. An exchange contribution was detected in the transverse relaxation rate (R_2) of all residues. The differential temperature response of R_2 along the backbone supported slower exchange rates for residues in the loop ($\tau_{ex} > 300$ μs) than for the folded polypeptide chain ($\tau_{ex} < 150$ μs). The distribution of the reduced spectral densities at the ^{1}H and ^{15}N frequencies followed the dynamic trend and predicted the slowing of the internal motions at 10 °C. Comparison of the dynamics with those of the holoprotein [Dangi, B., Sarma, S., Yan, C., Banville, D. L., and Guiles, R. D. (1998) *Biochemistry 37*, 8289−8302] demonstrated that binding of the heme alters the time scale of motions both in the heme-binding loop and in the structured hydrophobic core.

The dynamic nature of native protein structures is expressed in a variety of internal motions ranging from local fluctuations of atoms or side chains (*1*, *2*) to large-scale conformational changes associated with rigid body displacement of entire domains (*3*). The functional importance of some of these motions has been elucidated in enzymatic action (*4*), ligand entry and binding (*5*), and protein−protein (*6*) and protein−DNA recognition (*7*), to name but a few examples. The corresponding time scales range from a few picoseconds (rapid fluctuations about an average structure) to milliseconds and slower (transition between conformations). This broad spectrum of molecular motions can be probed by ^{1}H-detected ^{13}C and ^{15}N NMR relaxation measurements (*8*, *9*). The most common dynamic analyses are used to investigate the amide N−H bonds.

Nonfunctional species, such as molten globules, partially folded proteins, and unfolded proteins, are important for gaining insight into the determinants of protein folding and stability (*10*, *11*), but comparatively little is known about their internal motions. In practice, these flexible states are among the most challenging for dynamic characterizations (*12*−*19*). A special group of partially folded proteins includes those obtained by removal of an embedded prosthetic group. *b*-type hemoproteins are particularly interesting in this respect because of the steric properties of the heme and the unique topological features required of the apoproteins for efficient binding. Apocytochrome b_5 is selected here for its α/β fold and its favorable NMR characteristics.

Cytochrome b_5 serves as an electron carrier in a number of physiological processes (*20*, *21*). The water-soluble domain of the membrane-bound microsomal cytochrome b_5 (cyt b_5)[1] is a globular protein whose single heme group is attached to the polypeptide chain through two Fe−His coordination bonds. The X-ray structure of the oxidized bovine isoenzyme (*22*) reveals the key elements of the cyt b_5 fold (Figure 1A) (*23*). The heme-binding pocket (forming hydrophobic core 1) is predominantly α helical. It is adjacent to a second hydrophobic core, core 2, formed by an irregular β barrel and two terminal helices. Removal of the heme group is accompanied by partial loss of structure (*24*) and thermodynamic stability (*25*). The average low-resolution NMR structure of rat liver apocyt b_5 is shown in Figure 1B (*26*). In the apoprotein, core 2 remains largely intact while core 1 becomes a partially disordered loop encompassing

† This work was supported by National Institutes of Health Grant GM-54217.

* To whom correspondence should be addressed: Department of Chemistry, The Pennsylvania State University, 152 Davey Laboratory, University Park, PA 16802. Telephone: (814) 863-1153. Fax: (814) 863-8403. E-mail: jtl1@psu.edu.

[1] Abbreviations: apocyt b_5, apoprotein of the water-soluble fragment of hepatic cytochrome b_5; cyt b_5, heme-containing, water-soluble fragment of hepatic cytochrome b_5; CPMG, Carr−Purcell−Meiboom−Gill; CSA, chemical shift anisotropy; CT-$R_{1\rho}$, constant time off-resonance longitudinal relaxation rate constant in the rotating frame; DD, dipole−dipole; FID, free induction decay; HSQC, heteronuclear single-quantum coherence; HSMQC, heteronuclear single-multiple-quantum coherence; MD, molecular dynamics; NOE, nuclear Overhauser effect; NOESY, NOE spectroscopy; PDB, protein data bank; R_1, longitudinal relaxation rate constant; R_2, transverse relaxation rate constant; *T*, temperature; TOCSY, total correlation spectroscopy; TPPI, time-proportional phase incrementation; WATERGATE, water suppression by gradient-tailored excitation.

10.1021/bi982316d CCC: $18.00
Published on Web 02/04/1999

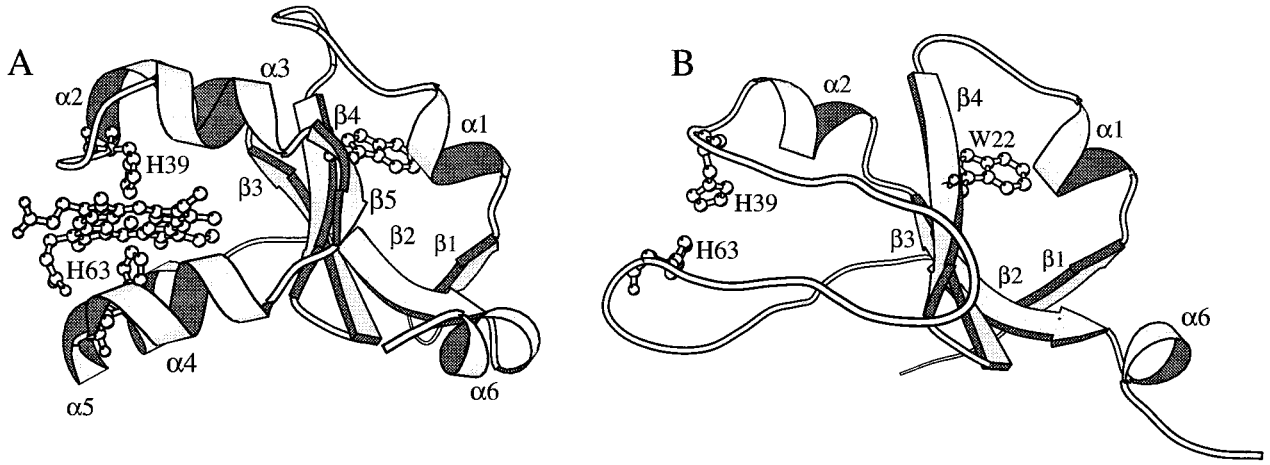

FIGURE 1: (A) Ribbon diagram of the X-ray structure of bovine cyt b_5 in the oxidized state (1cyo) (*22*). The heme, ligating histidines (His-39 and His-63), and Trp-22 are shown in ball-and-stick representations. Core 1 refers to the set of hydrophobic side chains lining the heme-binding pocket. Core 1 is part of "module 1", formed by the secondary structure elements α2−α3−β5−α4−α5. Core 2 contains Trp-22 and side chains from α1, α6, and strands β1−β4. These elements constitute "module 2". (B) Schematic representation of the average NMR structure of rat apocyt b_5 (1iet) (*26*). Little structure remains in module 1, whereas module 2 is mostly folded. The disordered heme-binding loop extends from residue 40 to 70, and is referred to in the text as the hb loop. The figures were generated using MOLSCRIPT (*23*); the β strands in cyt b_5 are labeled in the customary fashion according to the topology, not the primary structure.

30 residues. Surface loops in folded proteins are shorter on average. They have multiple purposes, from setting up the connectivity between consecutive secondary structural elements to enabling biological function. The unusual length of the apocyt b_5 loop is required for establishing a sufficient number of heme contacts in the holoprotein.

Several properties of apocyt b_5 require a dynamic study to complement the structural determination. (i) A useful representation of the flexible heme-binding loop should include its internal motions. (ii) The region containing core 1 (module 1) and that containing core 2 (module 2) have been treated as independent on the basis of structural and kinetic studies (*27*). Yet, when the heme-binding segment is excised from the sequence, an abridged version of the protein is obtained which folds with low stability (*28*). The autonomy of the two modules and the dynamic coupling between them are therefore open to investigation. (iii) The thermal unfolding of apocyt b_5, as followed by calorimetry of the rabbit protein (*25*) and verified by optical probes restricted to core 2 in the rat protein (ref *28* and this work), is modeled satisfactorily with a cooperative transition between a native state (N) and an unfolded state (U). The temperature response of the dynamics is expected to elucidate the onset of thermal denaturation in each module. (iv) Addition of the heme consolidates the structure of the protein in module 1 (*26*). Comparing apocyt b_5 and cyt b_5 data (*29*, *30*) will reveal original information about the entropic consequences of binding the heme. (v) Molecular dynamics simulations of apocyt b_5 indicate conformational heterogeneity as well as increased mobility in module 1 (*31*). Experimental data may reflect these features and validate the calculations.

A large portion of the backbone of apocyt b_5 can be monitored by NMR spectroscopy, including the segment delineating the heme-binding site. Thus, it is a priori possible to compare the time scale of the motions in the two regions of the protein. In this first apocyt b_5 dynamics study, data are presented for ^{15}N relaxation in the native state. It is found that the folded and the disordered regions sample different motional regimes. The dynamic view of the structure allows for a clearer understanding of the consequences of heme binding.

MATERIALS AND METHODS

Protein Samples. Uniformly ^{15}N-enriched rat liver holocyt b_5 was prepared with recombinant techniques as described elsewhere (*26*). The method of Teale (*32*) was followed for preparing the apoprotein. NMR data were collected in 90% H_2O/10% ^2H_2O at either pH 6.2 or 7.7 and between 10 and 25 °C. The labeled protein concentration was estimated to be ≈1 mM by comparing one-dimensional NMR spectra of the samples of interest to those of unlabeled samples with known concentrations determined by UV spectroscopy (ϵ_{280} = 10.6 M^{-1} cm^{-1}). Additional data were acquired on an ≈0.3 mM sample at pH 7.7 and 25 °C.

NMR Spectroscopy. NMR data were acquired on a Bruker AMX2-500 spectrometer (11.7 T, operating at a ^{1}H frequency of 500.13 MHz and a ^{15}N frequency of 50.68 MHz) and a Bruker DRX-600 spectrometer (14.1 T, operating at a ^{1}H frequency of 600.13 MHz and a ^{15}N frequency of 60.81 MHz). Typical acquisition parameters included 2048 complex points for sampling the spectral width along the direct (^{1}H) dimension and 160−256 real points along the indirect (^{15}N) dimension. A total of 64 transients were collected for each t_1 increment. The TPPI method (*33*) was used for frequency discrimination in the indirect dimension. The spectral widths for the ^{15}N and ^{1}H dimensions were 30 and 14 ppm, respectively. The center of the ^{15}N spectral width was 119 ppm, and the ^{1}H carrier was placed at the water peak.

The laboratory frame R_1, R_2, and NOE relaxation spectra were recorded according to established methods (*34*, *35*) suitably modified to incorporate the WATERGATE sequence (*36*) for solvent suppression. The data collected at pH 6.2 and 25 °C differed in the use of a conventional low-power pulse for solvent presaturation during the recycling delay. Typically, 8−10 spectra were collected in random order with

the variable relaxation delays ranging between 20 and 800 ms for R_1 measurements and between 7 and 150 ms for R_2 measurements. Several time points were repeated two to three times to estimate the intensity errors. The R_2 data sets at 14.1 T and 25 °C were recorded with the delays between the refocusing pulses of the CPMG pulse train set to either 1000 or 400 μs. Decoupling of the protons during the inversion recovery delay in the R_1 experiment was achieved with hard 180° proton pulses spaced at intervals of 5 ms. Additional data were acquired with selective cosine-shaped pulses to minimize the perturbation of the solvent during decoupling (*37*). R_1, $R_{1\rho}$, and R_2 experiments were carried out with a 3 s recycling delay to reduce sample heating. For the heteronuclear NOE experiments, the recycle delay was 4 s and included a 3 s period for saturation of the amide protons with a GARP-1 sequence (*38*).

Constant time off-resonance rotating frame relaxation (CT-$R_{1\rho}$) data were acquired following the method of Akke and Palmer (*39*). At 11.7 T, the ^{15}N magnetization was spin-locked with a radiofrequency field of strength 2330 Hz applied at an offset of 46 ppm from the center of the ^{15}N spectral width (119 ppm). At 14.1 T, the data were collected at two different offsets (23 and 46 ppm) from the center of the ^{15}N spectral width with a spin-lock field strength of 1560 Hz. The constant relaxation period T was set to 300 ms, and spectra were collected at eight variable spin-lock times (from 7 to 275 ms).

^{1}H−^{15}N three-dimensional (3D) NOESY−HSQC and ^{1}H−^{15}N 3D TOCSY−HSQC spectra were collected at 14.1 T, pH 7.7, and 25 °C as described previously (*26*) with spectral parameters adjusted for the higher magnetic field. ^{1}H−^{15}N HSQC spectra were also recorded at pH 6.2 and at 15, 20, 25, and 30 °C. To determine the tautomeric state of the histidines in apocyt b_5, ^{1}H−^{15}N HSMQC (*40*) spectra were recorded at 14.1 T under the following pH and temperature conditions: pH 6.2 and 25 °C and pH 7.7 and 10, 25, and 35 °C. The acquisition parameters along the two dimensions were as follows: ^{1}H spectral width of 14 ppm centered at the water signal described by 2048 complex points and ^{15}N spectral width of 150 ppm centered at 225 ppm, described by 256 complex points [TPPI−States quadrature detection (*41*)]. For selective observation of long-range ^{1}H−^{15}N correlation of the histidines ($^2J_{NH} = 6-12$ Hz), the refocusing delay in the INEPT sequence was set to 21.7 ms.

Data Processing. The ^{1}H−^{15}N correlation spectra were processed with FELIX 97.0 (Molecular Simulations Inc., San Diego, CA). Typically, the raw data in the time domain were convoluted with a Gaussian function to remove the residual solvent signal. The FIDs were corrected for the first point and zero-filled up to 4096 points before transformation. For resolution enhancement, the data were multiplied by a sine-squared window function with a phase shift of 54°. Minor baseline distortions were corrected by subtracting a zero- or first-order fitted polynomial function. The ^{15}N interferograms were extended to 256 points by linear prediction before apodizing with a sine-squared window function phase-shifted by 75°. The size of the transformed matrix was 2048 × 2048 real points. Proton chemical shifts were indirectly referenced to DSS through the water signal with temperature correction (*42*). ^{15}N chemical shifts were referenced indirectly to liquid NH_4Cl (*43*). Intensities of the individual peaks were measured for the various time points for each relaxation data set.

Determination of the Relaxation Rate Constants. The relaxation rate constants, R_1 (longitudinal) and R_2 (transverse), were obtained by fitting the peak height versus time profiles to a monoexponential decay function (*35*, *44*)

$$I_t = I_o \exp(-R_i t) + I_\infty \quad (1)$$

In the above equation, R_i ($i = 1$ or 2) is the rate constant, t is the variable relaxation delay, I_t is the intensity measured at time t, I_o is the intensity at time zero, and I_∞ is the final intensity. The uncertainty associated with the measurement of peak heights was determined as the standard deviation of the difference in peak heights obtained for all the resolved peaks from duplicate spectra recorded at the lowest relaxation delay, divided by $2^{1/2}$ (*44*). For each residue, the adequacy of a two-parameter fit (I_o and R_i) over a three-parameter fit (I_o, I_∞, and R_i) was judged from the 95% confidence limits of a χ^2 goodness-of-fit test and an F-test where necessary. The data were fit by using the optimization routines based on the Levenberg−Marquardt algorithm available in the Curvefit facility of the Modelfree 4.0 software (A. G. Palmer, III). The reported uncertainties in the relaxation rate constants are those obtained from the fit and are comparable to standard deviations obtained through Monte Carlo simulations. The NOE was calculated as the ratio of the intensity measured with and without saturation of the amide protons. The reported standard deviations were obtained indirectly from the root-mean-square baseplane noise or directly from three separate measurements.

At pH 6.2 and 25 °C, R_1 and NOE values were determined for 74 out of 92 residues at 11.7 T. Because of resonance offset effects in the CPMG experiment and severe line broadening, the R_2 values of only 54 residues were measured reliably under these experimental conditions. At pH 7.7 and 25 °C, the three relaxation parameters were obtained at 14.1 T for 61 residues, except for two residues where R_2 could not be determined by the CPMG experiment owing to scatter in the data. The data collected at 11.7 T for the same sample yielded all the relaxation parameters for 60 residues.

The rate constant for relaxation in the rotating frame ($R_{1\rho}$) was obtained by fitting the measured intensities to

$$I(t) = \hat{I}_o \exp(-R_{eff} t) \quad (2)$$

with

$$R_{eff} = (R_2 - R_1) \sin^2 \theta \quad (3)$$

In eq 2, $\hat{I}_o$ is given by $\exp(-R_1 T)$, where T represents the constant relaxation period, and in eq 3, θ is the tilt angle between the reduced static field and the effective field in the rotating frame (*39*). The R_2 values were determined by using the measured R_{eff} and R_1 values. The standard deviation in the calculated R_2 was obtained through propagation of errors.

Reduced Spectral Density Mapping. The principal mechanisms of relaxation of the amide ^{15}N involve dipole−dipole coupling to the attached proton and chemical shift anisotropy (*45*). In the absence of cross-correlation effects, the R_1, R_2, and ^{1}H−^{15}N NOE parameters are expressed as functions of

the spectral density $J(\omega)$ at five different frequencies of NMR transition as indicated in eqs 4−8.

$$R_{1,\mathrm{DD+CSA}} = \frac{1}{4}d_{\mathrm{NH}}^2[J(\omega_{\mathrm{H}} - \omega_{\mathrm{N}}) + 3J(\omega_{\mathrm{N}}) + 6J(\omega_{\mathrm{H}} + \omega_{\mathrm{N}})] + \frac{1}{3}\omega_{\mathrm{N}}^2(\sigma_{||} - \sigma_{\perp})^2 J(\omega_{\mathrm{N}}) \quad (4)$$

$$R_{2,\mathrm{DD+CSA}} = \frac{1}{8}d_{\mathrm{NH}}^2[4J(0) + J(\omega_{\mathrm{H}} - \omega_{\mathrm{N}}) + 3J(\omega_{\mathrm{N}}) + 6J(\omega_{\mathrm{H}}) + 6J(\omega_{\mathrm{H}} + \omega_{\mathrm{N}})] + \frac{1}{18}\omega_{\mathrm{N}}^2(\sigma_{||} - \sigma_{\perp})^2[4J(0) + 3J(\omega_{\mathrm{N}})] \quad (5)$$

$$R_2 = R_{2,\mathrm{DD+CSA}} + R_{\mathrm{ex}} \quad (6)$$

$$\mathrm{NOE} = 1 + \frac{1}{4R_1}d_{\mathrm{NH}}^2\frac{\gamma_{\mathrm{H}}}{\gamma_{\mathrm{N}}}[6J(\omega_{\mathrm{H}} + \omega_{\mathrm{N}}) - J(\omega_{\mathrm{H}} - \omega_{\mathrm{N}})] \quad (7)$$

$$d_{\mathrm{NH}} = \frac{h\mu_0}{8\pi^2}\gamma_{\mathrm{H}}\gamma_{\mathrm{N}}\left\langle\frac{1}{r_{\mathrm{NH}}^3}\right\rangle \quad (8)$$

In these equations, ω_{N} and ω_{H} are the Larmor frequencies of the ^{15}N and ^{1}H nuclei, respectively, $\sigma_{||}$ and $\sigma_{\perp}$ are the parallel and perpendicular components of the axially symmetric ^{15}N chemical shift tensor, respectively, γ_{H} and γ_{N} are the gyromagnetic ratios of ^{15}N and ^{1}H nuclei, respectively, h is Planck's constant, μ_0 is the permeability of free space, and r_{NH} (1.02 Å) is the N−H bond length. The numerical value of the difference $\sigma_{||} - \sigma_{\perp}$ was set to −160 ppm for the peptide bond and −89.6 ppm for the indole N−H bond (*46*). The R_{ex} term in eq 6 is phenomenological and accounts for microsecond (μs) to millisecond (ms) conformational exchange contributions to R_2.

The reduced spectral density mapping approach assumes $J(\omega)$ is a constant in the frequency range defined by $\omega_{\mathrm{H}} \pm \omega_{\mathrm{N}}$ (*47*). Solving for the spectral densities from the three relaxation parameters expressed as functions of $J(\omega_{\mathrm{H}})$, $J(\omega_{\mathrm{N}})$, and $J(0)$ is then straightforward. The values of $J(\omega_{\mathrm{H}})$ and $J(\omega_{\mathrm{N}})$ were calculated from data acquired at both B_{o} fields and temperatures. $J(0)$, which contains exchange contributions, was not used. The uncertainty in $J(\omega)$ was set equal to the standard deviation obtained from fitting 500 simulated data sets. The estimate of the random error from the Monte Carlo simulations of the spectral densities is less than 1%, whereas the uncertainty obtained by error propagation was higher by a few percent.

Model-Free Analysis. In the extended model-free (EMF) analysis (*48*, *49*), $J(\omega)$ is given an expression dependent on two time scales at least 1 order of magnitude apart. The EMF approach was simplified further by neglecting the contribution of the fast (less than 10 ps) time scale to the spin relaxation. The analytical form of the EMF spectral density function is

$$J(\omega) = \left[\frac{S^2\tau_{\mathrm{m}}}{1 + (\omega\tau_{\mathrm{m}})^2} + \frac{S_{\mathrm{f}}^2(1 - S_{\mathrm{s}}^2)\tau_{\mathrm{s}}'}{1 + (\omega\tau_{\mathrm{s}}')^2}\right] \quad (9)$$

with

$$\frac{1}{\tau_{\mathrm{s}}'} = \frac{1}{\tau_{\mathrm{m}}} + \frac{1}{\tau_{\mathrm{s}}} \quad (10)$$

where τ_{m} is the isotropic global correlation time of the molecule, S_{f}^2 and S_{s}^2 are the order parameters for the fast (τ_{f}) and slow motions (τ_{s}), respectively, and $S^2 = S_{\mathrm{f}}^2S_{\mathrm{s}}^2$ is the generalized order parameter, that is, a measure of the degree of spatial restriction of the amide bond vector. For a single time scale motion, S_{f}^2 is equal to unity and eq 9 assumes the form proposed by Lipari and Szabo (*48*). Calculations were performed using the Modelfree 4.0 programs. The R_1 and ^{1}H−^{15}N NOE data acquired at both B_{o} fields and 25 °C were fit simultaneously to this model. The R_2 values measured at 14.1 T were excluded from the analysis because of their high uncertainty. An R_{ex} term was included in the model to reproduce the high R_2 of all the residues. The reported standard deviations associated with the results were obtained from the fit using the Brent method of nonlinear optimization and are comparable to the values obtained from standard deviation of 300 Monte Carlo simulations.

Determination of the Global Correlation Time (τ_m). Fitting the relaxation data within the MF framework requires an initial estimate of the global correlation time for subsequent selection of the appropriate motional model of the N−H bond vector (*50*). In the absence of an independent estimate of rotational correlation time, τ_{m} may be extracted from the R_2/R_1 ratio (*34*, *51*) averaged over the entire backbone. The limitation of this approach lies in the assumption of a rigid N−H bond vector undergoing isotropic motion. Incorrect estimates of τ_{m} are obtained if either chemical exchange or motions on the picosecond to nanosecond time scale are present and ignored in the relaxation constants. Since there is sufficient reason to suspect the presence of both types of motions along the backbone of apocyt b_5, no attempt was made to apply the model selection strategies dependent on fixing τ_{m} (*52*). For similar reasons, the anisotropy could not be estimated from the predicted relaxation constants using the average NMR structure (*53*). Instead, the optimization used a crude grid search to find a global τ_{m} (for isotropic motion) and the dynamic parameters τ_{e} and S^2 for individual residues. These parameters served as a starting point for subsequent refinement.

The anisotropy of the structure was evaluated by performing hydrodynamic calculations based on a bead model with a modified Oseen tensor (*54*). The average NMR structures was hydrated to within a maximum distance of 3.5 Å from the surface of the protein by using the CHARMm routines of the Quanta program (Molecular Simulations Inc.). The translation and rotational diffusion constants of the solvated structure were calculated with the program HYDRO (*54*), for which the protein heavy atoms (N, Cα, and C′) and the water O atoms were replaced by beads assigned a radius of 1.0 and 1.6 Å, respectively (*55*). The calculations were repeated with a Cα-only representation of the protein (bead radius of 3.5 Å).

UV−Vis Spectroscopy. The thermal denaturation of apocyt b_5 was monitored by UV−vis spectroscopy on an AVIV 14DS UV−vis spectrophotometer. The samples, contained in 1 cm path length cuvettes, were 0.024 mM protein in 20

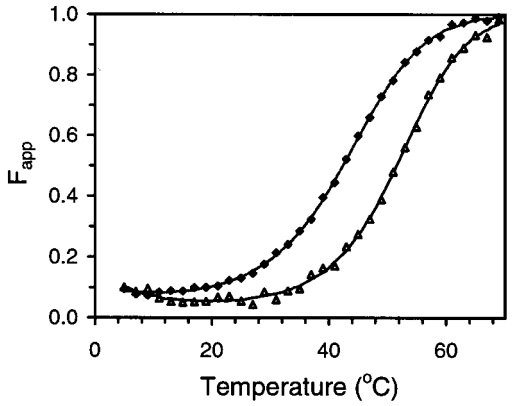

FIGURE 2: Plot of the apparent fraction of unfolded protein (F_{app}) vs temperature derived from thermal denaturation experiments. Samples were 0.024 mM apocyt b_5 in 20 mM phosphate buffer at pH 8.0 (◆) and 6.2 (△). The absorbance was monitored at 285 nm. The lines represent a two-state fit using the parameters listed in the text.

mM phosphate buffer adjusted to pH 6.2 or 8.0. Spectra were collected between 260 and 320 nm every 2 °C between 5 and 69 °C, with a 5 min interval between scans for thermal equilibration. Returning the sample to the starting temperature and comparing initial and final spectra led to a reversibility of better than 95%. Data were fitted to a two-state model of denaturation to obtain an estimate of thermodynamic parameters (*28*, *56*).

RESULTS AND DISCUSSION

Temperature and pH Dependence of the Native State. Relaxation measurements were performed at pH 6.2 and 7.7 and 25, 15, or 10 °C. The backbone amide ^{1}H and ^{15}N chemical shifts at pH 6.2 and 25 °C are as previously published (*26*). At pH 7.7, the ^{1}H−^{15}N HSQC spectrum was reassigned by using ^{1}H−^{15}N NOESY−HSQC and ^{1}H−^{15}N TOCSY−HSQC data. The persistence of the ^{1}H−^{1}H NOE connectivity patterns demonstrates that no major conformational rearrangement is caused by the change in pH. A few minor differences in chemical shifts were observed that could be attributed to the proximity of a titrating histidine side chain. The cross-peaks at 10 °C were assigned by following the chemical shift as a function of temperature in a series of HSQC spectra collected between 25 and 10 °C.

One of the concerns for the interpretation of the NMR data is the structural integrity of the apoprotein under variable sample conditions. The resistance to thermal and pH-induced denaturation of the apoprotein was investigated by absorption spectroscopy. The reversible transition between native (N) and unfolded (U) states can be fitted with a two-state model and yielded thermodynamic parameters that agree with those obtained by monitoring the loss in secondary structure by CD spectroscopy (*28*). The standard Gibbs energy of unfolding at 25 °C changes from 7 ± 1 kJ mol^{-1} at pH 6.2 to 5 ± 1 kJ mol^{-1} at pH 8.0. The fraction of unfolded protein at pH 6.2 and 8.0 is plotted as a function of temperature in Figure 2. Approximately 95% of the protein is native at pH 6.2 and 25 °C. At pH 8.0, 87% of the protein is folded at 25 °C and 92% at 10 °C. Therefore, the native protein is the predominant species under the chosen experimental conditions, and a small fraction of unfolded protein is always present according to the two-state model.

^{1}H−^{15}N NOE, ^{15}N R_1, and ^{15}N R_2 Relaxation Measurements. Figure 3 illustrates the field and temperature dependence of the ^{1}H−^{15}N NOE, R_1, and R_2 values measured at pH 7.7 along the backbone of apocyt b_5. At 11.7 T, the standard deviation obtained from the fits to the intensity-versus-time profiles was typically 1% (R_1), 5% (R_2), and 8% (^{1}H−^{15}N NOE). Comparable numbers were obtained at the higher B_o field. The standard deviations from the fits underestimate the actual errors by a few percent because of the broad lines and pulse lengths. All values are listed in Tables S1 and S2 of the Supporting Information.

The heteronuclear ^{1}H−^{15}N NOE is most sensitive to backbone dynamics for proteins with a global correlation time on the nanosecond time scale (*34*). Thus, a rigid amide N−H bond vector tumbling isotropically with a correlation time of 5 ns is characterized by an NOE of 0.75, whereas unrestricted motions result in a value of −3.62. In apocyt b_5, the average NOE values for residues 6−40 and 70−84 is 0.71 at pH 7.7 and 25 °C (Figure 3A). Systematically lower NOE values are obtained for the unstructured loop formed by residues 40−70 (hb loop) and the termini. This observation is consistent with a dynamic hb loop and termini attached to intact α/β secondary structure elements in module 2.

The longitudinal relaxation rate constant at 25 °C senses the motions of the termini and to a lesser extent those of the hb loop (Figure 3B). At 10 °C, the NOEs were found to increase for all residues compared to the values measured at 25 °C (Figure 3A), with the largest increase in the loop. In contrast, the R_1 values decrease at lower temperatures, and the decrease is minimal in the loop and the termini (Figure 3B).

For the holoprotein, the correlation time is between 5 and 6 ns, and the average R_2 value is 8 s^{-1} at 14.1 T (*30*) as expected for an 11.2 kDa protein (*57*). The R_2 values of apocyt b_5 (Figure 3C) are uniformly higher. This is indicative of the loss of phase coherence through chemical exchange as expressed in eq 6. Often, the identification of a non-zero R_{ex} term relies on detectable line broadening for selected residues. The situation is not obvious if all NH correlation peaks are similarly affected. For apocyt b_5, relaxation by chemical exchange on intermediate (microsecond to millisecond) time scales appeared to involve the entire backbone. Conformational exchange is not surprising in the flexible loop but requires confirmation in the folded regions of the protein. The prospect of a monomer−dimer or multimer equilibrium with a millimolar dissociation constant was considered. Association is often revealed by changes in chemical shift or line width upon dilution (*62*, *63*). No such spectroscopic evidence was detected in apocyt b_5. To probe this further in relationship to dynamic properties, the relaxation rates R_1 and R_2 were compared at 1 and 0.3 mM apoprotein. The response is consistent with a slight decrease in viscosity and incompatible with a large shift in overall correlation time. Ultracentrifugation data for the rat protein (0.2 mM, in the presence of 0.1 M NaCl, data not shown) and the calf protein [0.045 mM, in the presence of 0.1 M phosphate (*24*)], along with size-exclusion chromatography and differential scanning calorimetry data for the rabbit protein (*25*), suggest that the highly conserved hb loop does not promote association in the sub-millimolar concentration range. The state of aggregation of the unfolded protein in

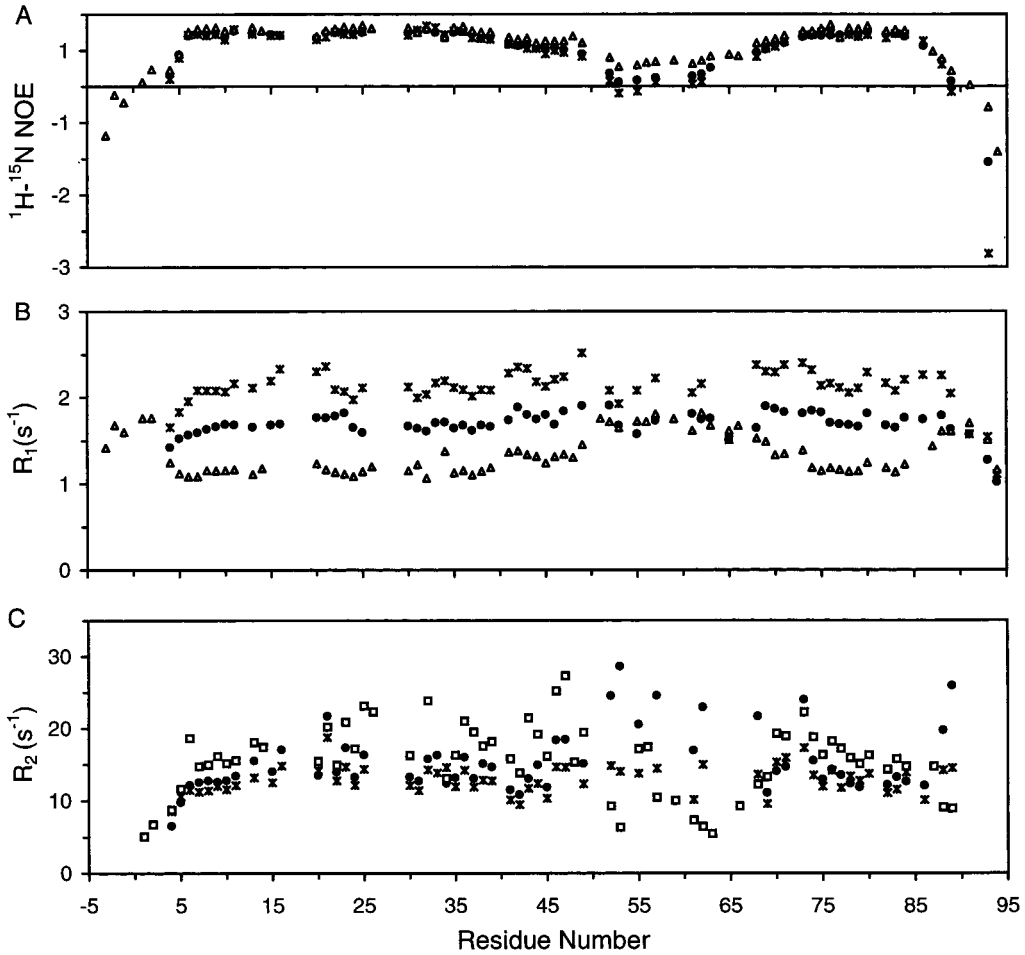

FIGURE 3: ^{15}N relaxation parameters as a function of residue number for apocyt b_5 at pH 7.7. The rat sequence starts at residue −4 and ends at residue 94 for alignment reasons: (A) ^{1}H−^{15}N NOE, (B) R_1 (s^{-1}), and (C) R_2 (s^{-1}). The different symbols refer to data acquired at (∗) 11.7 T and 25 °C, (●) 14.1 T and 25 °C, (△) 14.1 T and 10 °C, and (□) 14.1 T and 15 °C. Error bars are not included in the figure for clarity. Individual values are listed in the Supporting Information.

equilibrium with the native species remains undetermined. However, its low concentration can only lead to minor effects. Thus, the data analysis focuses on a native monomeric species with an R_{ex} due to intramolecular processes. This key aspect of apocyt b_5 was investigated by changing the acquisition parameters and temperature.

To reduce the uncertainty in the R_2 measurements introduced by line broadening at 10 °C, data were collected at 15 °C. Figure 3C illustrates that temperature has a differential effect on the response of R_2 values. Several residues in the hb loop and termini (52, 53, 57, 61, 62, 88, and 89) show an increase in R_2 measured at 25 °C (●) compared to that measured at 15 °C (□). This response deviates from the trend presented by the rest of the backbone, which shows a decrease in R_2 with T. The interpretation of these data relies partly on the ability to distinguish the effect of temperature on R_{ex} when superimposed on picosecond to nanosecond time scale motions.

Conformational Exchange on the Microsecond to Millisecond Time Scale. Techniques for the identification and evaluation of R_{ex} include changing the refocusing delay in the CPMG experiment (*58*) or varying the amplitude of the spin-lock field applied to the ^{15}N magnetization in the rotating frame (*59*). The off-resonance CT-$R_{1\rho}$ experiment (*50*) offers advantages over these methods in probing conformational fluctuations on the microsecond to millisecond time scale. When the exchange can be approximated with a two-site mechanism, the following equations apply:

$$A \underset{k_r}{\overset{k_f}{\rightleftharpoons}} B \tag{11}$$

$$K = \frac{k_f}{k_r} = \frac{p_B}{p_A} \tag{12}$$

$$k_{ex} = k_f + k_r \tag{13}$$

where K is the equilibrium constant, p_A and p_B are the fractional populations of the exchanging species, k_f and k_r are the forward and reverse reaction rate constants, respectively, and k_{ex} ($1/\tau_{ex}$) is the rate constant of exchange. The exchange rate measured in the CT-$R_{1\rho}$ experiment is given by

$$R_{ex,SL} = \frac{(\Delta\omega)^2 p_A p_B \tau_{ex}}{(1 + \tau_{ex}^2 \omega_e^2)} \tag{14}$$

In this equation, $\Delta\omega$ is the difference in ^{15}N chemical shifts between the exchanging species and ω_e is the effective field in the rotating frame. For a CPMG-based experiment (*60*),

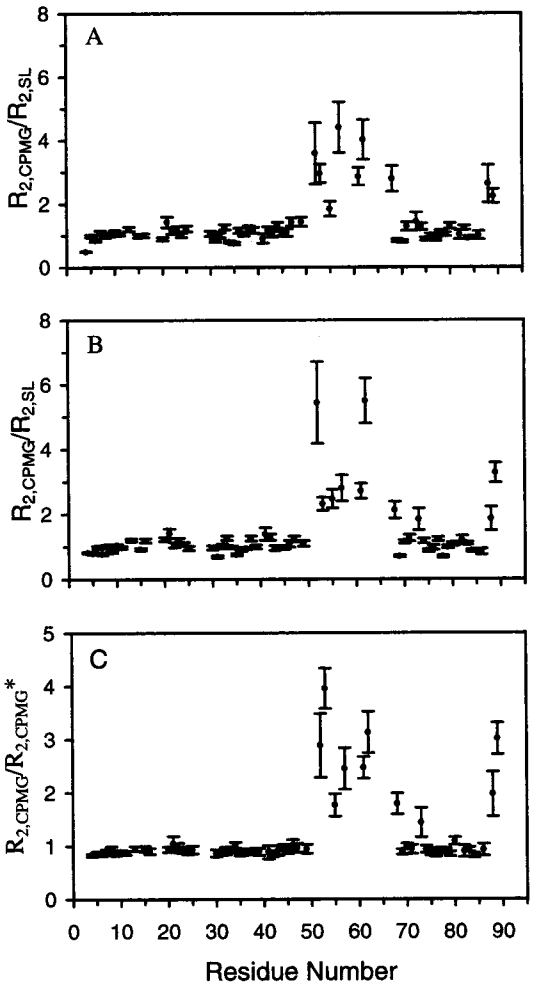

FIGURE 4: Ratio of R_2 values obtained with different acquisition parameters. (A) $R_{2,CPMG}/R_{2,SL}$ ratio at 11.7 T, with a τ_{CPMG} of 1 ms. $R_{2,SL}$ was derived from $R_{1\rho}$ data recorded with an offset of 46 ppm from the center of the ^{15}N spectral width at 119 ppm. (B) The same $R_{2,CPMG}/R_{2,SL}$ ratio at 14.1 T. (C) $R_{2,CPMG}/R_{2,CPMG*}$ ratio at 14.1 T, with τ_{CPMG} values of 1 ms ($R_{2,CPMG}$) and 0.4 ms ($R_{2,CPMG*}$). The data displayed in all three panels refer to those recorded at pH 7.7 and 25 °C. Error bars were calculated by the propagation method. Data were not obtained for terminal residues because of line broadening.

the R_{ex} term takes the following form:

$$R_{ex,CPMG} = p_A p_B (\Delta\omega)^2 \tau_{ex}\left[1 - \frac{2\tau_{ex}}{\tau_{CPMG}}\tanh\left(\frac{\tau_{CPMG}}{2\tau_{ex}}\right)\right] \quad (15)$$

where τ_{CPMG} is the delay between the refocusing pulses of the CPMG train. This expression reproduces the exchange parameters with reasonable accuracy if $\Delta\omega < 4.00$ ppm and $k_{ex}\tau_{CPMG} > 0.01$ (*61*). The ratio of the total R_2 values determined by the two methods

$$\frac{R_{2,CPMG}}{R_{2,SL}} = \frac{R_{2,DD+CSA} + R_{ex,CPMG}}{R_{2,DD+CSA} + R_{ex,SL}} \quad (16)$$

may therefore vary from unity in the presence of exchange. The experimental R_2 ratios obtained for apocyt b_5 at 11.7 and 14.1 T are plotted in panels A and B of Figure 4, respectively. Although the error is large for some residues, the deviation from unity in the hb loop and the C-terminus is significant and indicates participation in exchange processes.

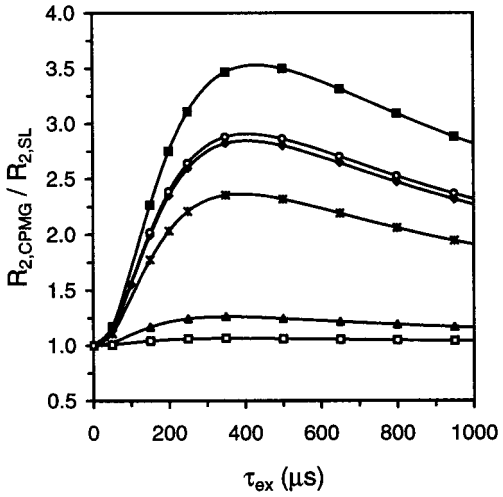

FIGURE 5: Variation of the ratio $R_{2,CPMG}/R_{2,SL}$ as a function of the exchange rate simulated for a two-site process. The curves correspond to different combinations of exchange parameters used to generate R_{ex} according to eqs 14 and 15: (◆) $\Delta\omega = 3$ ppm, $p_A p_B = 0.09$, and $R_{2,DD+CSA} = 6$ s^{-1}; (■) $\Delta\omega = 3$ ppm, $p_A p_B = 0.09$, and $R_{2,DD+CSA} = 4$ s^{-1}; (∗) $\Delta\omega = 1.5$ ppm, $p_A p_B = 0.25$, and $R_{2,DD+CSA} = 6$ s^{-1}; (○) $\Delta\omega = 1.5$ ppm, $p_A p_B = 0.25$, and $R_{2,DD+CSA} = 4$ s^{-1}; (□) $\Delta\omega = 0.5$ ppm, $p_A p_B = 0.09$, and $R_{2,DD+CSA} = 6$ s^{-1}; and (▲) $\Delta\omega = 0.5$ ppm, $p_A p_B = 0.25$, and $R_{2,DD+CSA} = 4$ s^{-1}.

The theoretical range of values adopted by $R_{2,CPMG}/R_{2,SL}$ was explored by calculating R_{ex} terms with plausible sets of exchange parameters. In these simulations, τ_{CPMG} was kept at 1 ms and ω_e at 2 kHz. The parameter p_A was set at 0.9 (predominance of one site) or 0.5 (equal population of the two sites), while $\Delta\omega$ was varied from 0.5 and 3 ppm and τ_{ex} from 50 μs to 1 ms. The exchange terms so generated were added to the pure $R_{2,DD+CSA}$ expected of a rigid (6 s^{-1}) or dynamic (4 s^{-1}) N−H bond vector with a τ_m of 5 ns. The resulting $R_{2,CPMG}/R_{2,SL}$ ratios, shown in Figure 5, are between ca. 0.9 and 3.5.

Figure 5 shows that several interpretations are possible for the ratio values near 1 exhibited by module 2. However, when $\Delta\omega$ is larger than 1 ppm, a near-unity value can be obtained only if the N−H bond vectors participate in exchange processes with a τ_{ex} of <150 μs ($k_{ex} > 6000$ s^{-1}). This is likely for N−H bonds outside of the hb loop since large $R_{2,CPMG}$ values imply a sizable $\Delta\omega$ (eq 15). Within the hb loop, the higher ratio can be ascribed to the lower-limit $R_{2,DD+CSA}$ values (which reflect sub-nanosecond dynamics, 200 ps < τ_e < 900 ps) in conjunction with R_{ex} terms generated with a τ_{ex} of >300 μs ($k_{ex} < 3300$ s^{-1}). If the experiment is repeated with a shorter τ_{CPMG} (400 μs) at 25 °C, the rates are scarcely affected in module 2 (Figure 4C). The small change is reminiscent of the fast exchange effect observed in a fragment of bacteriorhodopsin, where R_{ex} was monitored for different spin-echo periods (*58*). The marked decrease in $R_{2,CPMG}$ in the hb loop is in agreement with a slow exchange process with rates near the maximum of the curve described by eq 15. This experiment supports the distinctly different dynamic nature of the two modules. Further quantitative comparison of experimental and simulated values would require estimates of populations and chemical shift differences.

The variability in the exchange rates along the backbone must be consistent with the changes in $R_{2,CPMG}$ with temperature (Figure 3C). As T is raised, the accelerated tumbling

of the molecule depresses $R_{2,DD+CSA}$ via the $J(0)$ contribution in eq 5. In contrast, $R_{ex,CPMG}$ is a complex function of several variables linked by the thermodynamic properties of the exchanging system, and it may either decrease or increase as T is raised. The function $R_{ex,CPMG}(T)$ can be cast with eq 15, rewritten to include the temperature dependence of τ_{ex} derived from the Arrhenius relation. For a two-state process,

$$k_{ex} = A_f \exp\left(-\frac{E_f}{RT}\right) + A_r \exp\left(-\frac{E_r}{RT}\right) \qquad (17)$$

where E_f and E_r are the activation energies of the forward and backward reactions, respectively, and define the standard change in enthalpy $\Delta H°$ ($E_f - E_r$). The fractional populations of A and B vary according to eq 12 and

$$K(T) = \exp\left[-\frac{\Delta G°(T)}{RT}\right] \qquad (18)$$

which expresses the equilibrium constant through the standard Gibbs energy change for the process, $\Delta G°(T)$. R is the gas constant. Expansion of $\Delta G°(T)$ yields (*56*)

$$\Delta G°(T) = \Delta H°(T_m)\left[1 - \frac{T}{T_m}\right] - \Delta C_p°\left[(T_m - T) + T\ln\left(\frac{T}{T_m}\right)\right] \qquad (19)$$

where T_m is the midpoint of the thermal transition, $\Delta H°(T_m)$ is the standard enthalpy change at T_m, and $\Delta C_p°$ is the heat capacity difference between A and B, assumed to be independent of T.

The temperature response of $R_{ex,CPMG}$ was simulated for various activation energies assuming the pre-exponential factors to be equal and approaching the Eyring limit of 10^{12} s^{-1}. In all cases, k_f was smaller than k_r, and E_f was larger than $\Delta H°$; k_{ex} was bound by a practical upper limit of 10^6 s^{-1}. The ^{15}N chemical shift difference ($\Delta\omega$) was set equal to 1 ppm and τ_{CPMG} to 1 ms. Two situations are considered and shown in Figure 6.

(i) $\Delta H° = 0$, $\Delta C_p° = 0$, and $k_f = k_r$. In this simple case, the product $p_A p_B$ in eq 15 is a constant. Figure 6A displays $R_{ex,CPMG}$ as a function of temperature for E_f values ranging between 48 and 61 kJ mol^{-1}. $R_{ex,CPMG}(T)$ has a maximum for $k_{ex}\tau_{CPMG}$ of 3.2, and consequently, inspection of the slope at any temperature suffices to predict the experimental k_{ex} with respect to the reference value of $3.2/\tau_{CPMG}$ (3200 s^{-1} in this case).

(ii) $\Delta H° = 35$ kJ mol^{-1}, $\Delta C_p° = 0$, and $\Delta S° = 100$ J K^{-1} mol^{-1}. This corresponds to a temperature-sensitive equilibrium, with a maximum in the function $p_A p_B$ at 77 °C. Unlike in the previous situation, the temperature at which $R_{ex,CPMG}$ reaches its highest value does not necessarily correspond to a $k_{ex}\tau_{CPMG}$ of 3.2, and the time scale of exchange is not readily derived from $dR_{ex,CPMG}/dT$. For example, if $E_f = 57$ kJ mol^{-1}, the maximum occurs when $k_{ex}\tau_{CPMG} = 4$, whereas if $E_f = 52$ kJ mol^{-1}, it occurs when $k_{ex}\tau_{CPMG} = 12$. Further complexity is introduced if $\Delta C_p°$ is non-zero, as observed for the global cooperative unfolding transition. Therefore, estimating k_{ex} with $dR_{ex,CPMG}/dT$ data requires additional information about the equilibrium, and the analysis for apocyt b_5 yields only broad k_{ex} ranges.

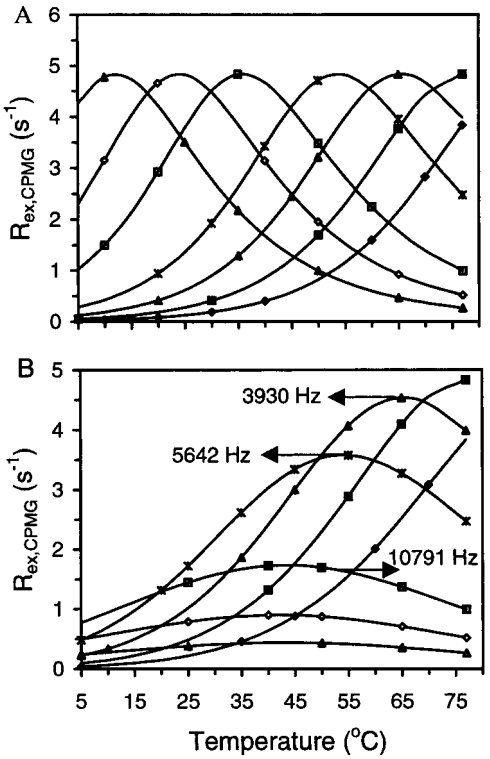

FIGURE 6: Simulated temperature dependence of R_{ex}: (A) $\Delta H° = 0$, $\Delta S° = 0$, and $\Delta C_p° = 0$, corresponding to a T-independent $p_A p_B$ of 0.25, and (B) $\Delta H° = 35$ kJ mol^{-1} and $\Delta S° = 100$ J mol^{-1} K^{-1}, corresponding to a transition with a midpoint of 77 °C. Exchange rates were calculated using the $\Delta H°$ values above and the following E_f values (see the text): (◆) 61, (■) 59, (▲) 57, (∗) 55, (□) 52, (◇) 50, and (△) 48 kJ mol^{-1}. The numbers in panel B indicate the k_{ex} values at the R_{ex} maximum, assuming $\tau_{CPMG} = 1$ ms. In panel A, the k_{ex} value at the maximum is 3200 s^{-1} regardless of E_f.

Two proteins for which conclusions could be reached serve as extreme examples: ribonuclease H in its native state (*50*) and a low-stability fragment of staphylococcal nuclease (*12*). The ribonuclease H results are consistent with conformational fluctuations on a fast time scale leading to a decrease in $R_{ex,CPMG}$ as the temperature is increased. The nearly equal and low forward and reverse activation energies qualify the process as type i above. In contrast, the dynamics of the staphylococcal nuclease fragment show an increase in R_{ex} as the temperature is increased. This corresponds to a slow, two-site exchange associated with the unfolding of the native form.

As pointed out above, the hb loop of apocyt b_5 displays an increase in total transverse relaxation time with temperature (Figure 3C). The responsible increase in $R_{ex,CPMG}$ suggests slow exchange between two sets of conformers. The possibility that one of these sets is the unfolded form was inspected by simulations using the thermodynamic parameters of the thermal denaturation [$\Delta H°(T_m) = 136$ kJ mol^{-1}, $\Delta C_p° = 4$ kJ mol^{-1} K^{-1}, and $T_m = 46$ °C]. The $R_{ex,CPMG}$ resulting from this equilibrium is small because of the low value of $p_A p_B$ below 25 °C (less than 0.07) and high $\Delta H°$ above 27 °C (greater than 60 kJ mol^{-1}). The latter sets the upper limit on k_{ex} at 400 s^{-1}, which would not be detectable. Slow exchange rates (2000 $s^{-1} < k_{ex} < 4000$ s^{-1}) with $p_A p_B$ approaching 0.25 can account for the magnitude and direction of the change in R_{ex} terms at 25 °C. In contrast to the hb loop, the folded region of the protein exhibits a decrease in $R_{ex,CPMG}$ with T. The response is consistent with a fast process

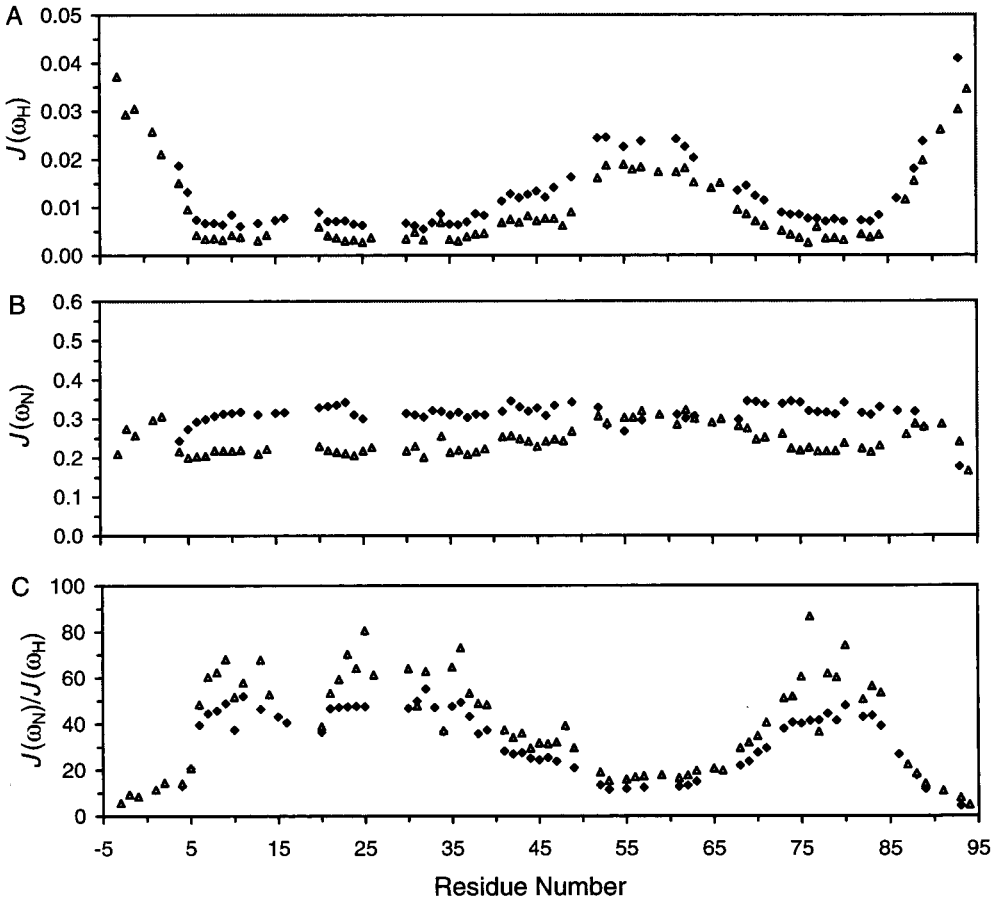

FIGURE 7: Reduced spectral density profiles in ns/rad at the frequency of ^{1}H [$J(\omega_H)$, A] and that of ^{15}N [$J(\omega_N)$, B]. Panel C illustrates the ratio $J(\omega_N)/J(\omega_H)$. Data for apocyt b_5 at pH 7.7 and 14.1 T are shown at (△) 10 and (◆) 25 °C. Error bars are obscured by the data point symbols.

(3000 $s^{-1} < k_{ex} < 10\,000\ s^{-1}$). The ranges of k_{ex} obtained with the temperature response reinforce the conclusions of the R_2 ratio analysis.

The preceding discussion has rested on fast to intermediate exchange rates on the chemical shift time scale, as prescribed by the observation of a single peak for most amides. There is also some evidence of slow exchange giving rise to minor peaks in the spectra. The chemical identity of the exchanging species has been assigned to conformational heterogeneity in the C-terminal helix α6 and part of strand β2 (*64*). This process is too slow to be detected in the CPMG experiment ($k_{ex} < 100\ s^{-1}$). In summary, the variation of the relaxation parameters along the polypeptide chain of apocyt b_5 reflects picosecond to nanosecond time scale motions superimposed on temperature-activated exchange processes. The nature of these dynamic processes can be explored by analyzing the data within the framework of the model-free approach or the spectral density mapping approach.

Spectral Density Mapping. The spectral densities evaluated at the frequency of NMR transitions reflect the range of time scales sampled through the motion of the N−H bond vector. The variation in $J(\omega_H)$ and $J(\omega_N)$ across the backbone of apocyt b_5 is displayed in Figure 7A,B and follows the distribution of 1 − NOE and R_1, respectively (Figure 3A,B). The close correspondence between the profiles is explained by the predominant $J(\omega)$ term in the expression for the relaxation parameter (*57*).

The ability to probe the dynamics of the N−H bond through the spectral densities measured at various frequencies follows from the conservation of the total area under $J(\omega)$, which is proportional to the mean-squared energy of the bond motions driving the various relaxation mechanisms (*45*). Therefore, a comparison of $J(\omega)$ measured at high and low frequencies provides a quantitative measure of the breadth of the frequency distribution accessed through the spatial fluctuations of the bond and the overall tumbling of the molecule. For instance, a broad distribution with significant contributions to the area from high frequencies would indicate the presence of fast internal motion on the order of a few hundred picoseconds. On the other hand, a narrow distribution indicates that slow molecular tumbling is the principal contributor to $J(\omega)$. Typically for proteins with well-defined structures, the higher intensity of the low-frequency components of $J(\omega)$ reflects the sensitivity of the N−H vector to the slow rotational correlation time on the order of a few nanoseconds. However, conformational averaging may alter the $J(\omega)$ profile significantly and shift the dominant time scale from τ_m to the sub-nanosecond regime.

For apocyt b_5 at 25 °C, $J(\omega_H)$ and $J(\omega_N)$ are consistent with the hb loop and termini undergoing motions on the sub-nanosecond time scale. The broad shape for $J(\omega)$ in the mobile regions is characterized by lower-than-average $J(\omega_N)$ values for residues 50−68 and terminal residues 4−9, 88, 89, and 93. This trend is partly offset by $J(\omega_H)$, which shows a systematic increase for residues 4, 5, 86, 88, 89, 93, and those between 40 and 73. The observed profiles at 25 °C are strikingly different from those at 10 °C, where $J(\omega_H)$ and $J(\omega_N)$ display enhanced values in the loop compared to

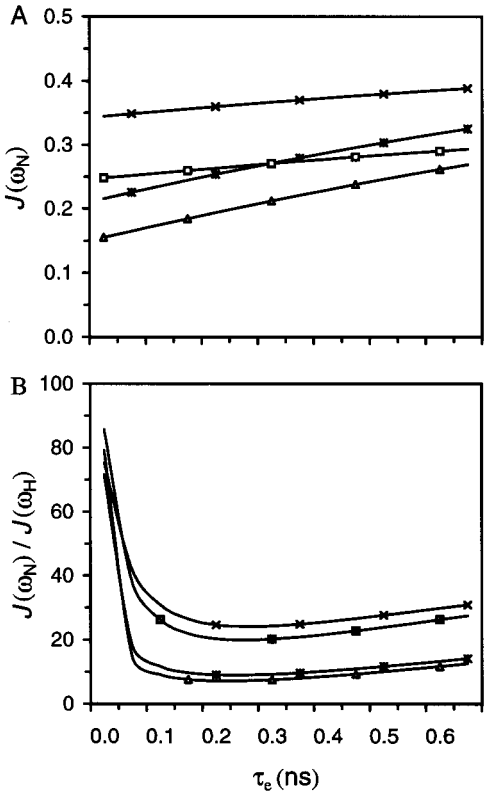

FIGURE 8: Simulated spectral density at the ^{15}N frequency and the ratio of $J(\omega_N)/J(\omega_H)$ as a function of the internal correlation time τ_e (ns) for the following motional parameters: (×) $S^2 = 0.8$ and $\tau_m = 5$ ns, (□) $S^2 = 0.8$ and $\tau_m = 8$ ns, (∗) $S^2 = 0.5$ and $\tau_m = 5$ ns, and (△) $S^2 = 0.5$ and $\tau_m = 8$ ns.

those in the remaining backbone. In addition, $J(\omega_N)$ increases near the termini at positions 1 and 2 and 88 and 89 and undergoes a monotonic decrease toward positions −3 and 94.

The dynamic model appropriate for a rigid backbone scales all correlation times as a function of the solvent viscosity at different temperatures. Typically, the decrease in $J(\omega_N)$ with temperature for all S^2 and τ_e of less than 1 ns is predicted to be on the order of 0.01 unit if τ_m is in the nanosecond time scale regime (*65*). This decrease is smaller by a factor of 10 than the observed difference of 0.1 in structured regions of apocyt b_5. It is appropriate to assume that the dominant motion of the N−H vectors in the rigid portions of the backbone is due to the molecular tumbling and reflected by the $J(\omega_N)$ values. To conserve the total area under $J(\omega)$, an increase of 2−3 ns in τ_m brought about by the decrease in temperature to 10 °C would depress $J(\omega_N)$ significantly by increasing $J(0)$ compared to the same values at 25 °C. In the hb loop, the alteration of the spectral density profile through a τ_m effect is also coupled to the slowing of the internal motion. The effect of the various factors on the relative change of the spectral densities was explored through simulation of $J(\omega_N)$ and the correlation of spectral densities at two frequencies $J(\omega_N)/J(\omega_H)$ (*7*) for τ_m values of 5 and 8 ns, and for all combinations of S^2 and τ_e. The results of the calculations are displayed in Figure 8. The choice of τ_m was arbitrary given the absence of an estimate from an alternate source (τ_m for the holoprotein is 4.5 ns). Figure 8A shows the expected increase in $J(\omega_N)$ with increasing τ_m.

The ratio $J(\omega_N)/J(\omega_H)$ is more sensitive to internal motion on the picosecond time scale (<100 ps) because of the disproportionately larger changes in $J(\omega_H)$ compared to those in $J(\omega_N)$ (Figure 8B). With reference to Figure 7C, the $J(\omega_N)/J(\omega_H)$ values for residues in the hb loop and termini are smaller than those in the remainder of the protein at 10 and 25 °C. This observation is in agreement with local subnanosecond dynamics. The steep change in $J(\omega_N)/J(\omega_H)$ with temperature in the folded portion of the backbone reflects predominantly the quenching of the internal motion on a time scale faster than 100 ps. The effect of temperature is minimal as the limit of slow (greater than 150 ps) internal motion is approached in the loop and termini.

The rationale for the above arguments is also compatible with the uniform increase in $J(\omega_H)$ with temperature, which reflects the transition to fast motion. The effect of τ_m on $J(\omega_H)$ is smaller than that on $J(\omega_N)$ for comparable values of S^2 and τ_e and therefore not obvious from the differences at the two temperatures. The test of the increase in τ_m is generally the ratio of $J(0)$ values at the two temperatures; this method is not recommended in this case because of the contribution from chemical exchange.

Model-Free Calculations. The relaxation data were also analyzed using the MF approach of Lipari and Szabo for isotropic motion. The N−H vectors participating in regular secondary structure are characterized by high S^2 (0.75−0.87) and low τ_e values (less than 50 ps). The average standard deviation for S^2 and τ_e is less than 1 and 20%, respectively. The final estimate of τ_m was equal to 5.5 ns. Most of the residues were fitted to the simple three-variable model (S^2, τ_e, and R_{ex}) within 95% confidence limit with the exception of residues 4, 16, 89, and 93 in the termini and 49−62 in the loop. An attempt to fit these residues with the EMF approach outlined in eq 9 failed to improve the quality of the fit. This implies a complexity of motion ignored when a single global correlation time was used.

The anisotropy of the apocyt b_5 conformational ensemble could yield spurious R_{ex} and τ_e values. The axially symmetric anisotropy derived from the hydrated NMR structure equals 1.2 (beads centered on Cα) and 1.3 (beads centered on N, Cα, and C′). The corresponding translational diffusion coefficient equals 12.7×10^{-7} cm^2 s^{-1}, a value within the expected range for a molecule of this size (*56*). However, the eigenvalues of the rotational diffusion tensor remain dependent on the choice of parameters and structural model; they are unreliable unless they are calibrated against experimental data (*54*). The main limitation for a partially folded system is the lack of adequate representation for the flexible segments.

For a rigid nonspherical body, it has been demonstrated through fitting simulated data that R_2 is underestimated by 20% for anisotropies ($D_{||}/D_{\perp}$) equal to 2.0 (*66*). The effect on the correlation time is unique to the angle between the N−H bond vector and the axis of the diffusion tensor. For moderate anisotropies (ca. 1.3), the order parameters remain insensitive to the choice of model (*30*). Therefore, in the case of the average apoprotein structure, the estimated S^2 values afford a reasonable view of the N−H vector motions but the τ_e values may be overestimated. Individual structures have anisotropies below 2.0 as calculated by the same procedure. A fit to an anisotropic model (available in Modelfree 4.0) was not attempted because of exchange. The combined results of R_{ex} determination and internal motion analyses are listed in Table 1.

Table 1: Summary of Backbone Dynamics in Cytochrome b_5

	apoprotein	holoprotein[a]
hb loop[b]	100 ps $< \tau_e <$ 500 ps	$\tau_e <$ 50 ps
	$\tau_{ex} >$ 300 μs	$\tau_{ex} <$ 200 μs
module 2[c]	$\tau_e <$ 100 ps	$\tau_e <$ 50 ps
	$\tau_{ex} <$ 150 μs	

[a] Values taken from Kelly et al. (*29*) and Dangi et al. (*30*). [b] Residues 40−70 of the heme-binding loop. [c] Residues involved in secondary structure.

pH Dependence of the Relaxation Constants. The thermal stability of apocyt b_5 is slightly higher at pH 6.2 than at pH 7.7. To investigate the possible relation between the dynamics and stability of the apoprotein, the relaxation constants at 11.7 T were measured at pH 6.2 and 25 °C. The range and variation in $J(\omega_H)$ and $J(\omega_N)$ estimated from the relaxation constants were within error of those obtained at pH 7.7, suggesting that the motions of the backbone in the native state are not influenced by the 1.5 unit change in pH.

The effect of pH on the structure and stability of proteins is mostly through the titration of charged side chains. The tautomeric state of the histidines of apocyt b_5 was determined at pH 6.2 and 7.7 and 25 °C (*67*). The pattern of cross-peaks contains information about the tautomeric state in the neutral state via the four $^2J_{NH}$ correlations between imidazole ring ^{15}N and the nonexchangeable carbon-bound protons (*68*). Deprotonation occurs preferentially from the Nδ position and results in the formation of approximately 80% Nϵ tautomer at neutral pH. Of particular interest is the pH and temperature response of two helix-capping imidazoles: His-15 (a C-cap for helix α1) and His-80 (an N-cap for helix α6). Both side chains participate in stable tertiary interactions.

Previous NMR studies have indicated that His-80 either forms a capping hydrogen bond (major form, ~90%) or is free (minor form) (*64*). The equilibrium between the two forms is slow on the chemical shift time scale, and the heterogeneity is detected downstream through α6 and upstream in the last residues of β2. The major form of His-80 (pK_a < 5) involves exclusively the Nϵ tautomer, a consequence of hydrogen bond formation between the imidazole Nδ and the amide proton of Asp-82. The side chain to main chain hydrogen bond is resistant to increased fluctuations at higher temperatures. The minor form of His-80 is also detectable and displays the approximate 4:1 equilibrium mixture of tautomeric states generally observed for free histidine groups. The major form of His-80 describes the rigidity and structure of the N-cap of α6. Unfortunately, the information for the C-cap interaction between the His-15 NδH proton and the backbone carbonyl oxygen of Glu-11 is lost through line broadening during the titration (pK_a ≈ 8.0).

Dynamics of the Folded Module. The N-terminal segment (β1−α1−β4−β3−α2) and C-terminal segment (β2−α6) of module 2 are rigid on the sub-nanosecond time scale. The small-amplitude N−H bond librations (0.75 < S^2 and τ_e < 50 ps) are characteristic of hydrogen bond formation within the preserved secondary structural elements and an apolar environment sequestered from the solvent. These motions are decorrelated from the microsecond dynamics associated with the chemical exchange term. The indole NH of the single Trp of apocyt b_5 (Trp-22, Figure 1B) provides a probe for monitoring the dynamics of a conserved side chain within core 2. The limited mobility of the N−H bond (S^2 = 0.88) suggests a side chain frozen into a well-defined orientation.

The most dynamic stretch in the folded module is restricted to the turn connecting helix α1 and strand β4 (residues 13−20, corresponding to turns 1 and 2 in the holoprotein). Chemical exchange on the microsecond to millisecond time scale broadens the amide resonances of residues 17−19 beyond detection at pH 7.7. The onset of the slow dynamics is visible in the increase in the relaxation constants at the two tethered ends of these turns. The amide resonances are also broadened in turn 3 (residues 25−28, connecting strands β4 and β3), which contains His-26 and His-27. Histidine protonation−deprotonation equilibria are likely to contribute to the line width and mask the dynamic information. However, the His-26 backbone NH could be observed at 10 °C. Its ^{1}H−^{15}N NOE value of 0.8 suggests restricted mobility on the picosecond to nanosecond time scale. His-27 could be followed only at low pH, and its ^{1}H−^{15}N NOE of 0.8 at pH 6.2 also points to a rigid turn. This turn (turn 3) is essential for positioning strands β3 and β4 correctly. In the holoprotein, it has been assigned conformational exchange on time scales faster than 200 μs (*69*). More recent work suggests the direct involvement of at least two hydrophobic side chains, Val-23 and Leu-25 (strand β3), in controlling heme reorientation (*30*, *70*). A rigid turn in the apoprotein predisposes these residues in the final geometry.

Dynamics of the Heme-Binding Module. The apoprotein heme-binding site has enhanced flexibility, except in irregular helix α2 (Thr-33−Glu-38). Conformational heterogeneity is manifested in the transition to complex motion by the backbone from Pro-40 to Leu-70. The bell-shaped profile of $J(\omega_H)$ (Figure 7A) illustrates the diminishing effect of the rigid backbone as the N−H vectors are farther from either end of this segment. The relaxation constants of one of the two ligating histidines (His-39) could be evaluated reliably (S^2 = 0.77). The rest of the loop has S^2 values between 0.60 and 0.70, and τ_e values between 100 and 500 ps. These values agree with known motional parameters for unfolded (*16*, *37*, *71*) or partially folded (*15*, *18*, *19*) proteins.

The reorientation motions of peptide bonds in polymer chains are characterized by the configurational parameter C_∞ (*72*) and the associated persistence lengths (*73*). The limiting values reflect the stiffness of the chain over a short segment involving 2−10 bonds and are unique to the composition of the polymer. A long polypeptide chain can be visualized as several such statistical segments linked in succession. An analogous situation is identified with the unfolded state of proteins in solution, subject to the additional effect of amino acid conformational biases in the $\varphi-\psi$ space (*14*). The direct measure of these effects has been demonstrated through the profile of the relaxation parameters in polypeptide chains with different degrees of randomness. The interpretation of the experimental results entails factoring the length of the chain, amino acid composition (*14*), and nonlocal contacts (*74*). The length of the unstructured loop in apocyt b_5 is sufficient for a plateau to be reached where purely segmental motions dominate (55−65). However, weak NOEs indicate that the tip of the loop is spatially restricted with respect to module 2 (*26*). This illustrates that segmental motions (short-range effects) are compatible with transient long-range contacts.

The interpretation of multiple time scale dynamics in proteins generally relies on fluctuations between conformational substates such as random coil or folded chain. The continuum bracketed by these extremes is divided into a hierarchy of states (*75*) whose occupational probability depends on the Gibbs energy and its relation to external perturbations for a given set of experimental conditions. This type of analysis is particularly relevant to the partially folded apocyt b_5. The N−H bond librations (<50 ps) in the folded module imply a single potential energy minimum with fluctuations between nearly degenerate substates. The relevant energies are on the order of a few kilojoules per mole (*76*). The physical changes associated with these motions are local and involve bond vibration or small displacement within a cage composed of solvent and protein atoms (*1*). On the other hand, the longer time scale motions (>200 ps) in the heme-binding loop illustrate jumps between discrete states separated by a large activation barrier (*1*). These slow jumps may reflect the substantial energy required for concerted motions of the backbone when solvent and a small number of tertiary contacts offer a net resistance. These subnanosecond motions in the average native conformation are superimposed on the chemical exchange (microsecond to millisecond) between states further separated in the energy landscape (≈40 kJ mol^{-1} or more). The difference in these slow exchange rates parallels the difference in activation energies associated with the conformational substates that are accessible to the two modules.

CONCLUDING REMARKS

In a fully folded native protein, the backbone dynamics probed by the NMR relaxation measurements are predominantly a function of the rotational correlation time, τ_m, with internal motions reflecting small fluctuations about an average structure. For all practical purposes, these motions are decorrelated. In partially folded proteins, backbone rigidity and lasting side chain packing are not the dominant features any longer. The protein is best represented by a dynamic ensemble of conformers, where the correlation between the collective motions of small segments is necessary for maintaining a system amenable to subsequent chemistry. Conformational analysis is facilitated in structured proteins, where the dynamic models generated with MD simulations have been tested against experimental parameters (*77*). Such approaches remain to be generalized for partially folded proteins. The current MD simulations for native apocyt b_5 extend to 1.6 ns and reproduce the loss of structure and picosecond to nanosecond internal motions in core 1 (*31*). The simulations are uninformative with respect to the experimentally identified sub-millisecond motions.

The goals of the study included the characterization of coupling between the two structural units in apocyt b_5 and the consequences of heme binding. In *b* hemoprotein, the affinity is driven by enthalpy, which is partitioned into contributions from desolvating the heme in the apolar protein environment, forming the proximal histidine−Fe bond, and rearranging side chains in the active site (*78*, *79*). Little is known about the activation barrier associated with individual steps and the corresponding microscopic rates. However, the bimolecular rate of heme association in apocyt b_5 [4.5×10^7 M^{-1} s^{-1} (*80*, *81*)] serves for gauging the relevance of the heme-binding loop motions to the heme binding affinity.

The disordered apoprotein heme pocket displays motions on multiple time scales, which do not interfere with heme binding. They are only partially restrained when the prosthetic group is inserted [Table 1 (*29*, *30*, *69*)] as exchange on the microsecond time scale for several residues (42−52 and 65−75) lining the hydrophobic pocket persists after consolidation of module 1. Similar flexibility, albeit on a faster time scale (picosecond to nanosecond), has been identified through MD simulations of the holoprotein (*82*). In the calculations, the increased rigidity of module 1 has no apparent effect on module 2. In contrast, the experimentally observed microsecond exchange in module 2 of the apoprotein suggests a certain degree of cooperativity, as suggested by the loss of stability in the truncated protein with the heme-binding loop replaced by a short linker (*28*). The key factor in the interactions of the two modules could be the length of the hb loop, which has to be maintained in a conformation conducive to rapid collapse into the native structure around the heme. It appears that for the cyt b_5 fold, the dynamic allowances made in the heme-binding region compromise the stability of module 2 and its rigidity on the microsecond time scale through the weakening of tertiary contacts at the interface. Module 2 retains picosecond fluctuations similar to those in the holoprotein, thus minimizing entropy loss through induced fit upon heme binding and eliminating kinetic traps. This scaffold may be a minimal requirement for binding the large heme group and at the same time optimizing function.

ACKNOWLEDGMENT

We thank Aileen Constans for assistance in protein preparation and purification.

SUPPORTING INFORMATION AVAILABLE

Two tables listing the relaxation parameters, a figure depicting the HSQC data, a figure depicting the S^2 and τ_e parameters as a function of backbone position, and a figure depicting the histidine tautomeric state data. This material is available free of charge via the Internet at http://pubs.acs.org.

REFERENCES

1. Karplus, M., and McCammon, J. A. (1983) *Annu. Rev. Biochem. 52*, 263−300.
2. Williams, R. J. P. (1989) *Eur. J. Biochem. 183*, 479−497.
3. Gerstein, M., Lesk, A. M., and Chothia, C. (1994) *Biochemistry 33*, 6739−6749.
4. Epstein, D. M., Benkovic, S. J., and Wright, P. E. (1995) *Biochemistry 34*, 11037−11048.
5. Hodsdon, M. E., and Cistola, D. P. (1997) *Biochemistry 36*, 2278−2290.
6. Carr, P. A., Erickson, H. P., and Palmer, A. G., III (1997) *Structure 5*, 949−959.
7. Lefèvre, J.-F., Dayie, K. T., Peng, J. W., and Wagner, G. (1996) *Biochemistry 35*, 2674−2686.
8. Palmer, A. G., III, Williams, J., and McDermott, A. (1996) *J. Phys. Chem. 100*, 13293−13310.
9. Kay, L. E. (1998) *Nat. Struct. Biol. 5* (NMR Supplement), 513−517.
10. Dill, K. A., and Shortle, D. (1991) *Annu. Rev. Biochem. 60*, 795−825.
11. Shortle, D. R. (1996) *Curr. Opin. Struct. Biol. 6*, 24−30.
12. Alexandrescu, A. T., Jahnke, W., Wiltscheck, R., and Blommers, M. J. (1996) *J. Mol. Biol. 260*, 570−587.

13. Buck, M., Schwalbe, H., and Dobson, C. M. (1996) *J. Mol. Biol. 257*, 669−683.
14. Schwalbe, H., Fiebig, K. M., Buck, M., Jones, J. A., Grimshaw, S. B., Spencer, A., Glaser, S. J., Smith, L. J., and Dobson, C. M. (1997) *Biochemistry 36*, 8977−8991.
15. Brutscher, B., Brüschweiler, R., and Ernst, R. R. (1997) *Biochemistry 36*, 13043−13053.
16. Frank, M. K., Clore, G. M., and Gronenborn, A. M. (1995) *Protein Sci. 4*, 2605−2615.
17. Fong, S., Bycroft, M., Clarke, J., and Freund, S. M. (1998) *J. Mol. Biol. 278*, 417−429.
18. van Mierlo, C. P., Darby, N. J., Keeler, J., Neuhaus, D., and Creighton, T. E. (1993) *J. Mol. Biol. 229*, 1125−1146.
19. Barbar, E., Hare, M., Daragan, V., Barany, G., and Woodward, C. (1998) *Biochemistry 37*, 7822−7833.
20. Velick, S., and Strittmatter, P. (1956) *J. Biol. Chem. 221*, 265−275.
21. Vergères, G., and Waskell, L. (1995) *Biochimie 77*, 604−620.
22. Mathews, F. S., and Czerwinski, E. W. (1976) *The Enzymes of Biological Membranes*, Vol. 4, Plenum Press, New York.
23. Kraulis, P. (1991) *J. Appl. Crystallogr. 24*, 946−950.
24. Huntley, T. E., and Strittmatter, P. (1972) *J. Biol. Chem. 247*, 4641−4647.
25. Pfeil, W. (1993) *Protein Sci. 2*, 1497−1501.
26. Falzone, C. J., Mayer, M. R., Whiteman, E. L., Moore, C. D., and Lecomte, J. T. J. (1996) *Biochemistry 35*, 6519−6526.
27. Moore, C. D., and Lecomte, J. T. J. (1993) *Biochemistry 32*, 199−207.
28. Constans, A. J., Mayer, M. R., Sukits, S. F., and Lecomte, J. T. J. (1998) *Protein Sci. 7*, 1983−1993.
29. Kelly, G. P., Muskett, F. W., and Whitford, D. (1997) *Eur. J. Biochem. 245*, 349−354.
30. Dangi, B., Sarma, S., Yan, C., Banville, D. L., and Guiles, R. D. (1998) *Biochemistry 37*, 8289−8302.
31. Storch, E. M., and Daggett, V. (1996) *Biochemistry 35*, 11596−11604.
32. Teale, F. W. J. (1959) *Biochim. Biophys. Acta 35*, 543.
33. Marion, D., and Wüthrich, K. (1983) *Biochem. Biophys. Res. Commun. 113*, 967−974.
34. Kay, L. E., Torchia, D. A., and Bax, A. (1989) *Biochemistry 28*, 8972−8979.
35. Skelton, N. J., Palmer, A. G., III, Akke, M., Kördel, J., Rance, M., and Chazin, W. J. (1993) *J. Magn. Reson., Ser. B 102*, 253−264.
36. Sklenár, V., Piotto, M., Lepik, R., and Saudek, V. (1993) *J. Magn. Reson. 102*, 241−245.
37. Farrow, N. A., Zhang, O., Forman-Kay, J. D., and Kay, L. E. (1995) *Biochemistry 34*, 868−878.
38. Shaka, A. J., Barker, P. B., and Freeman, R. (1988) *J. Magn. Reson. 64*, 547−552.
39. Akke, M., and Palmer, A. G., III (1996) *J. Am. Chem. Soc. 118*, 911−912.
40. Zuiderweg, E. R. P. (1990) *J. Magn. Reson. 86*, 346−357.
41. Marion, D., Ikura, M., Tschudin, R., and Bax, A. (1989) *J. Magn. Reson. 85*, 393−399.
42. Wishart, D. S., Bigam, C. G., Yao, J., Abildgaard, F., Dyson, H. J., Oldfield, E., Markley, J. L., and Sykes, B. D. (1995) *J. Biomol. NMR 6*, 135−140.
43. Live, D. H., Davis, D. G., Agosta, W. C., and Cowburn, D. (1984) *J. Am. Chem. Soc. 106*, 1939−1941.
44. Palmer, A. G., III, Rance, M., and Wright, P. E. (1991) *J. Am. Chem. Soc. 113*, 4371−4380.
45. Abragam, A. (1961) *The Principles of Nuclear Magnetism*, Clarendon Press, Oxford, U.K.
46. Hiyami, Y., Niu, C.-H., Silverton, J. V., Bavoso, A., and Torchia, D. A. (1988) *J. Am. Chem. Soc. 110*, 2378−2383.
47. Farrow, N. A., Zhang, O., Szabo, A., Torchia, D. A., and Kay, L. E. (1995) *J. Biomol. NMR 6*, 153−162.
48. Lipari, G., and Szabo, A. (1982) *J. Am. Chem. Soc. 104*, 4546−4559.
49. Clore, G. M., Szabo, A., Bax, A., Kay, L. E., Driscoll, P. C., and Gronenborn, A. M. (1990) *J. Am. Chem. Soc. 112*, 4989−4991.
50. Mandel, A. M., Akke, M., and Palmer, A. G., III (1996) *Biochemistry 35*, 16009−16023.
51. Yao, S., Hinds, M. G., and Norton, R. S. (1998) *J. Magn. Reson. 131*, 347−350.
52. Mandel, A. M., Akke, M., and Palmer, A. G., III (1995) *J. Mol. Biol. 246*, 144−163.
53. Tjandra, N., Feller, S. E., Pastor, R. W., and Bax, A. (1995) *J. Am. Chem. Soc. 117*, 12562−12566.
54. de la Torre, J. G., and Bloomfield, V. A. (1981) *Q. Rev. Biophys. 14*, 81−139.
55. Venable, R. M., and Pastor, R. W. (1988) *Biopolymers 27*, 1001−1014.
56. Creighton, T. E. (1995) *Proteins, Structures & Molecular Properties*, 2nd ed., W. H. Freeman & Co., New York.
57. Dayie, K. T., Wagner, G., and Lefèvre, J.-F. (1996) *Annu. Rev. Phys. Chem. 47*, 243−282.
58. Orekhov, V., Pervushin, K. V., and Arseniev, A. S. (1994) *Eur. J. Biochem. 219*, 887−896.
59. Szyperski, T., Lüginbuhl, P., Otting, G., Guntert, P., and Wüthrich, K. (1993) *J. Biomol. NMR 3*, 151−164.
60. Allerhand, A., and Gutowsky, H. S. (1965) *J. Chem. Phys. 42*, 1587−1599.
61. Davis, D. G., Perlman, M. E., and London, R. E. (1994) *J. Magn. Reson., Ser. B 104*, 266−275.
62. Fairbrother, W. J., Liu, J., Pisacane, P. I., Sliwkowski, M. X., and Palmer, A. G., III (1998) *J. Mol. Biol. 279*, 1149−1161.
63. Fushman, D., Cahill, S., and Cowburn, D. (1997) *J. Mol. Biol. 266*, 173−194.
64. Lecomte, J. T. J., and Moore, C. D. (1991) *J. Am. Chem. Soc. 113*, 9663−9665.
65. Landry, S. J., Steede, N. K., and Maskos, K. (1997) *Biochemistry 36*, 10975−10986.
66. Schurr, J. M., Babcock, H. P., and Fujimoto, B. S. (1994) *J. Magn. Reson., Ser. B 105*, 211−224.
67. Moore, C. D., al-Misky, O. N., and Lecomte, J. T. J. (1991) *Biochemistry 30*, 8357−8365.
68. van Dijk, A. A., Scheek, R. M., Dijkstra, K., Wolters, G. K., and Robillard, G. T. (1992) *Biochemistry 31*, 9063−9072.
69. Banci, L., Bertini, I., Cavazza, C., Felli, I. C., and Kouloughliotis, D. (1998) *Biochemistry 37*, 12320−12330.
70. Mortuza, G. B., and Whitford, D. (1997) *FEBS Lett. 412*, 610−614.
71. Farrow, N. A., Zhang, O., Forman-Kay, J. D., and Kay, L. E. (1997) *Biochemistry 36*, 2390−2402.
72. Flory, P. J. (1953) *Principles of Polymer Chemistry*, Cornell University Press, Ithaca, NY.
73. Cantor, C. R., and Schimmel, P. R. (1980) *Biophysical Chemistry Part III: The Behavior of Biological Macromolecules*, W. H. Freeman & Co., San Francisco, CA.
74. Alexandrescu, A. T., Rathgeb-Szabo, K., Rumpel, K., Jahnke, W., Schulthess, T., and Kammerer, R. A. (1998) *Protein Sci. 7*, 389−402.
75. Frauenfelder, H., and McMahon, B. (1998) *Proc. Natl. Acad. Sci. U.S.A. 95*, 4795−4797.
76. McCammon, J. A., and Harvey, S. C. (1987) *Dynamics of Proteins and Nucleic Acids*, Cambridge University Press, New York.
77. Philippopoulos, M., Mandel, A. M., Palmer, A. G., III, and Lim, C. (1997) *Proteins: Funct., Struct., Genet. 28*, 481−493.
78. Hargrove, M. S., Barrick, D., and Olson, J. S. (1996) *Biochemistry 35*, 11293−11299.
79. Robinson, C. R., Liu, Y., Thomson, J. A., Sturtevant, J. M., and Sligar, S. G. (1997) *Biochemistry 36*, 16141−16146.
80. Vergères, G., Chen, D. Y., Wu, F. F., and Waskell, L. (1993) *Arch. Biochem. Biophys. 305*, 231−241.
81. Gruenke, L. D., Sun, J., Loehr, T. M., and Waskell, L. (1997) *Biochemistry 36*, 7114−7125.
82. Storch, E. M., and Daggett, V. (1995) *Biochemistry 34*, 9682−9693.

BI982316D